Proton core-beam system in the expanding solar wind: Hybrid simulations

Petr Hellinger[1,2] and Pavel M. Trávníček[1,2,3]

Abstract. Results of a two-dimensional hybrid expanding box simulation of a proton beam-core system in the solar wind are presented. The expansion with a strictly radial magnetic field leads to a decrease of the ratio between the proton perpendicular and parallel temperatures as well as to an increase of the ratio between the beam-core differential velocity and the local Alfvén velocity creating a free energy for many different instabilities. The system is indeed most of the time marginally stable with respect to the parallel magnetosonic, oblique Alfvén, proton cyclotron and parallel fire hose instabilities which determine the system evolution counteracting some effects of the expansion and interacting with each other. Nonlinear evolution of these instabilities leads to large modifications of the proton velocity distribution function. The beam and core protons are slowed with respect to each other and heated, and at later stages of the evolution the two populations are not clearly distinguishable. On the macroscopic level the instabilities cause large departures from the double adiabatic prediction leading to an efficient isotropization of effective proton temperatures in agreement with Helios observations.

1. Introduction

Thermal and nonthermal proton properties in the fast solar wind are not well understood. The protons are essentially collisionless but they do not follow the double adiabatic prediction; their perpendicular temperature decreases with distance more slowly, whereas the parallel temperature decreases faster than what is expected from the double-adiabatic prediction [*Marsch et al.*, 1982]. Proton velocity distribution functions are largely gyrotropic and are typically skewed carrying a heat flux along the magnetic field in the direction away from the Sun [*Marsch et al.*, 1982]. The proton heat flux (or its radial gradient) seems to be negligible for the proton thermal energetics. However, the proton heat flux is typically comparable to the corresponding saturation heat flux [*Marsch et al.*, 1982; *Hellinger et al.*, 2011] indicating a presence of nonnegligible secondary/beam population or a strongly distorted proton velocity distribution function [*Feldman et al.*, 1973]. Helios observations indeed show that the proton velocity distribution function in the fast solar wind can be typically regarded as a superposition of two populations, a more abundant, typically anisotropic core with perpendicular temperature greater the parallel one and a secondary/beam population drifting with respect to the core along the ambient magnetic field [*Marsch et al.*, 1982]. Helios observations indicate that the drift velocity between the core and the beam decreases with the distance roughly following the local Alfvén velocity. This effect is on the macroscopic level connected with a cooling of the total/effective parallel proton temperature [*Marsch and Richter*, 1987]. A transfer of the parallel energy to the perpendicular one may be partly responsible for the observed proton perpendicular heating [*Schwartz et al.*, 1981].

Processes responsible for the formation of the beam and for its deceleration with respect to the core are not well established [*Matteini et al.*, 2011]. Helios [*Marsch and Livi*, 1987; *Tu et al.*, 2004] and Ulysses [*Goldstein et al.*, 2000] data sets indicate a presence of beam-driven electromagnetic instabilities [parallel magnetosonic, oblique Alfvén, cf., *Montgomery et al.*, 1976; *Daughton and Gary*, 1998] based on a linear analysis assuming two drifting bi-Maxwellian velocity distribution functions. Such a linear analysis [*Marsch and Livi*, 1987] indicate even strongly unstable cases in contradiction with the theoretical expectations [cf., *Hellinger et al.*, 2006, in the case of proton temperature anisotropy]. The presence of the parallel magnetosonic instability is moreover indicated by a linear analysis based on the observed proton velocity distribution function [*Dum et al.*, 1980]. The beam-driven instabilities naturally reduce the relative beam-core velocity as a part of the saturation mechanism [*Daughton et al.*, 1999] and may be responsible for the beam deceleration. In the solar wind the plasma system starts in the stable region and the expansion may continuously drive the system unstable [*Matteini et al.*, 2011]. In this paper we investigate the evolution of the beam-core proton system using the hybrid expanding box model which self-consistently models the competition between the expansion and ion kinetic instabilities. Section 2 presents linear and quasi-linear expectation for relevant instabilities, section 3 presents the numerical model and its results. Finally, in section 4 we discuss the simulation results and compare them with observations.

2. Theoretical considerations

Proton velocity distribution functions in the fast solar wind typically exhibit two populations [*Marsch et al.*, 1982]: first one, nominally more abundant, called here core and a second one called here beam. The two populations can be described to some extend as two bi-Maxwellian distributions [*Goldstein et al.*, 2000] drifting with respect to each other along the ambient magnetic field. Such a description is a useful approximation to investigate linear stability of the system with respect to different instabilities. However, this approximation is not generally sufficient for resonant instabilities [*Dum et al.*, 1980; *Gary*, 1993] where the linear dispersion is largely determined by a small resonant portion of the velocity distribution function.

The proton distribution function consisting of two bi-Maxwellian velocity distributions drifting with respect to each other may be a source of free energy for many different instabilities. Temperature anisotropy of the (core and possibly also beam) protons can generate at least four electromagnetic instabilities [*Gary*, 1993; *Hellinger et al.*, 2006]: for $T_{\mathrm{p}\perp} > T_{\mathrm{p}\parallel}$ there are the proton cyclotron and mirror instabilities while for $T_{\mathrm{p}\perp} < T_{\mathrm{p}\parallel}$ there are the parallel and oblique fire hose instabilities (for the definitions of all symbol used here see Appendix C).

The secondary/beam population drifting with respect to the core protons may drive another set of electromagnetic instabilities

[1]Astronomical Institute, AS CR, Prague, Czech Republic
[2]Institute of Atmospheric Physics, AS CR, Prague, Czech Republic
[3]SSL, UC Berkeley, USA

0148-0227/12/2011JA016940$9.00

[*Daughton and Gary*, 1998, and references therein]; the most relevant ones are usually the parallel magnetosonic [*Montgomery et al.*, 1976] and oblique Alfvén [numbered as (I) by *Daughton and Gary*, 1998] instabilities. It is important to note that the parallel fire hose and the magnetosonic instabilities drive waves at the same branch and are related [cf., *Hellinger and Trávníček*, 2006; *Matteini et al.*, 2011]. *Daughton and Gary* [1998] studied the linear competition of the parallel magnetosonic and oblique Alfvén instabilities. They found that for a wide range of parameters the parallel magnetosonic instability is dominant. However, as the two instabilities depend differently on the many present parameters (core and beam densities and temperatures, differential velocity, and electron parameters) the oblique Alfvén instability becomes dominant for another wide range of parameters (e.g., for large beam density and/or small core temperatures). Moreover, these instabilities are typically resonant and their properties strongly depend on the details of the velocity distribution function in the resonant region. Usually only the three basic resonances, cyclotron, Landau and anomalous cyclotron ones, are relevant. The corresponding resonant velocities (for a wave with the real frequency ω_r and the parallel component of the wave vector $k_\parallel$) are given as

$$v_c = \frac{\omega_r - \omega_{\rm cp}}{k_\parallel} \quad v_L = \frac{\omega_r}{k_\parallel}, \quad v_{ac} = \frac{\omega_r + \omega_{\rm cp}}{k_\parallel}. \qquad (1)$$

The resonant particles may importantly contribute to the linear (Equation (A1)) as well as to the nonlinear/quasi-linear (Equation (B5)) properties of the plasma.

At the parallel propagation, the linear dispersion splits to three branches separating the cyclotron, anomalous cyclotron (Equation (A4)) and Landau resonances. The parallel fire hose and the magnetosonic instabilities interact through the anomalous cyclotron resonance [*Matteini et al.*, 2006] while the proton cyclotron instability interacts through the cyclotron resonance [*Gary et al.*, 1976].

At oblique propagation, the unstable waves can resonate through more than one resonance at the same time. For example, while the mirror nonpropagating mode resonate with particles mainly through the Landau resonance [*Kivelson and Southwood*, 1996; *Califano et al.*, 2008] the nonpropagating oblique fire hose resonate through both cyclotron and anomalous cyclotron resonances [*Hellinger and Trávníček*, 2008]. Let us here look at the case of the oblique Alfvén instability. For the following parameters,

$$n_{\rm p} = 0.9 n_{\rm e},\ n_{\rm b} = 0.1 n_{\rm e},\ v_{\rm bp} = 1.8 v_A,$$
$$\beta_{\rm p\parallel} = 0.2,\ \beta_{\rm b\parallel} = 0.1,\ T_{\rm p\perp}/T_{\rm p\parallel} = 1.8,\ T_{\rm b\perp}/T_{\rm b\parallel} = 1, \qquad (2)$$

the system is unstable with respect to the oblique Alfvén instability with the maximum growth rate $\gamma_{\max} \simeq 10^{-2}\omega_{\rm cp}$ at $k \simeq 0.8 v_A/\omega_{\rm cp}$ and $\theta_{kB} \simeq 50.8^{\rm o}$ having $\omega_r \simeq 0.38\omega_{\rm cp}$. In this case, the unstable waves resonate with the protons strongly through the anomalous cyclotron resonance. Furthermore, they resonate non-negligibly through the Landau resonance whereas the cyclotron resonance is rather weak. To estimate strengths of the different resonances one can calculate the impact of the most unstable mode on the initial proton velocity distribution function f_0 through the quasi-linear diffusion

$$\frac{\delta f}{\delta t} = \frac{\partial}{\partial v_\parallel}\left[D_{\parallel\parallel}\frac{\partial f_0}{\partial v_\parallel} + D_{\parallel\perp}\frac{\partial f_0}{\partial v_\perp}\right] + \frac{1}{v_\perp}\frac{\partial}{\partial v_\perp} v_\perp \left[D_{\perp\parallel}\frac{\partial f_0}{\partial v_\parallel} + D_{\perp\perp}\frac{\partial f_0}{\partial v_\perp}\right]. \qquad (3)$$

The diffusion coefficients D have been derived by *Kennel and Engelmann* [1966] and are given in a more explicit form in Appendix B. Figure 1 displays the result of such a calculation for the example case with the parameters given by Equation (2). The top left panel of Figure 1 shows the proton velocity distribution function f_0 as a function of $v_\parallel$ and $v_\perp$. The other three panels show the contribution of the most unstable mode to the quasi-linear diffusion $\delta f/\delta t$ given by Equation (3) near the cyclotron resonance (top right), the Landau resonance (bottom left), and the anomalous cyclotron resonance (bottom right) as functions of $v_\parallel$ and $v_\perp$. The solid curves show isocontours for $\delta f/\delta t > 0$ whereas the dotted curves show isocontours for $\delta f/\delta t < 0$. The dash-dotted lines denote the resonant velocities, v_c (cyclotron), v_L (Landau), and v_{ac} (anomalous cyclotron) given by Equation (1). Figure 1 gives only qualitative results, the isocontour levels on the different panels are arbitrary and independent. Figure 1 shows that the oblique Alfvén instability slows the resonant beam particles and heat them in the perpendicular direction, has a tendency to flatten the velocity distribution function along $v_\parallel$ in the Landau resonant region and heats in the perpendicular direction and accelerate the resonant core protons through the cyclotron resonance. On the quantitative level, the amplitudes of $|\delta f/\delta t|$ are strongest for the anomalous cyclotron resonance, weaker for the Landau resonance and they are the weakest for the cyclotron resonance.

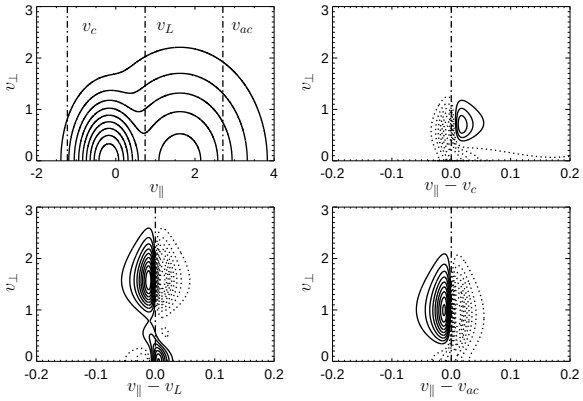

Figure 1. (top left) Example of unstable proton velocity distribution function f_0 as a function of $v_\parallel$ and $v_\perp$. The other panels show the contribution of the most unstable mode to the quasi-linear diffusion $\delta f/\delta t$ (Equation (3)) near the cyclotron resonance (top right), the Landau resonance (bottom left), and the anomalous cyclotron resonance (bottom right) as functions of $v_\parallel$ and $v_\perp$. The solid curves show isocontours for $\delta f/\delta t > 0$ whereas the dotted curves show isocontours for $\delta f/\delta t < 0$. Dashed dotted lines denote the resonant velocities, v_c, v_L, and v_{ac} (Equation (1)).

One can for a comparison calculate the impact of the most unstable mode for the magnetosonic instability and the result are qualitatively very similar to the anomalous cyclotron resonance of the oblique Alfvén instability (Figure 1, bottom right). In a case of a sufficient core temperature anisotropy $T_\perp > T_\parallel$ the proton cyclotron instability is destabilized and resonates through the cyclotron resonance. This instability has diffusion properties similar to those shown in Figure 1 (top right) but with the opposite effect $\delta f/\delta t \to -\delta f/\delta t$, cooling in the perpendicular direction and decelerating (resonant) core protons.

3. Simulation results

The two dominant beam driven instabilities, the parallel magnetosonic and oblique Alfvén ones, have different linear and nonlinear properties. They compete for essentially the same free energy. Their nonlinear behavior and competition is a highly complex problem which needs a kinetic modeling. *Daughton et al.* [1999] performed a set of standard two-dimensional (2-D) hybrid (kinetic ions and fluid electrons, see below) simulations and investigated and parametrized the saturation properties of these instabilities. They have assumed weakly unstable initial conditions and observed only weak wave amplitudes and small changes in the proton velocity

distribution functions which is compatible with the quasi-linear expectations. They have confirmed that these instabilities reduce the differential velocity between the beam and core and heat mainly the beam in the perpendicular direction.

3.1. Model and initial conditions

In standard numerical studies of kinetic instabilities the system starts in the unstable region and the simulation reveals the different instability phases, initial exponential grow, saturation and post-saturation evolution including effects of competition between different instabilities [*Daughton et al.*, 1999]. However, in the solar wind the system typically starts in the stable region and the expansion may continuously drive the system unstable [*Matteini et al.*, 2011]. To study the response of the solar wind plasma to a slow expansion we use in this paper the expanding box model [*Grappin et al.*, 1993] implemented to the hybrid code by *Matthews* [1994]. The Hybrid Expanding Box (HEB) simulations self-consistently model the competition between the expansion driven free energy for instabilities and the relaxation owing to these instabilities. In the HEB model [*Liewer et al.*, 2001; *Hellinger et al.*, 2003] the expansion is described as an external force where a constant solar wind radial velocity v_{sw} is assumed. The radial distance R is then

$$R = R_0 + v_{sw}t = R_0\left(1 + \frac{t}{t_e}\right) \tag{4}$$

where R_0 is an initial radial distance and $t_e = R_0/v_{sw}$ is a characteristic expansion time. Transverse scales (with respect to the radial direction) of a small portion of plasma, co-moving with the solar wind velocity, increase with time $\propto (1 + t/t_e)$. The expanding box uses these co-moving coordinates, replacing the spatial dependence by the temporal one (Equation (4)). The physical transverse scales of the simulation box increase with time [see *Hellinger and Trávníček*, 2005, for a detailed description of the code].

The characteristic spatial and temporal units used in the model are $v_A/\omega_{\rm cp0}$ and $1/\omega_{\rm cp0}$, respectively (for the definitions of symbols used here see Appendix C). We use the spatial resolution $\Delta x = \Delta y = v_A/\omega_{\rm cp0}$, and there are $2,048$ particles per cell for the core protons and $1,024$ particles per cell for the proton beam. Fields and moments are defined on a 2-D x–y grid with dimensions 512×512 with the periodic boundary conditions. Protons are advances using the Boris' scheme with a time step $\Delta t = 0.05/\omega_{\rm cp0}$, while the magnetic field $\boldsymbol{B}$ is advanced with a smaller time step $\Delta t_B = \Delta t/10$. The initial ambient magnetic field is directed along the radial, x direction, $\boldsymbol{B}_0 = (B_0, 0, 0)$ and we impose a continuous expansion in the transverse (y and z) directions.

For simplicity we here only consider a strictly radial magnetic field. In this case the expansion leads to a decrease of the ambient density and magnitude of the magnetic field as

$$n \propto B \propto \left(1 + \frac{t}{t_e}\right)^{-2} \tag{5}$$

and the double adiabatic prediction of the proton temperature anisotropy and parallel beta in the expanding box is

$$\frac{T_{\rm p\parallel}}{T_{\rm p\perp}} \propto \beta_{\rm p\parallel} \propto \left(1 + \frac{t}{t_e}\right)^{2}. \tag{6}$$

The expansion tends to increase $T_{\rm p\parallel}/T_{\rm p\perp}$ leading to the corresponding temperature anisotropy driven instabilities [*Hellinger and Trávníček*, 2008]. Furthermore, the Alfvén velocity decreases $v_A \propto 1/(1 + t/t_e)$ whereas the parallel differential velocity $v_{\rm bp}$ between the proton core and beam populations is constant (for the strictly radial magnetic field) when no wave activity or collisions are present. This results in a continuous increase of their ratio,

$$\frac{v_{\rm bp}}{v_A} \propto 1 + \frac{t}{t_e}, \tag{7}$$

which leads to beam driven instabilities.

For initial conditions we have chosen these parameters:

$$n_{\rm p} = 0.9n_{\rm e},\ n_{\rm b} = 0.1n_{\rm e},\ v_{\rm bp} = 1.3v_A,$$
$$\beta_{\rm p\parallel} = 0.2,\ \beta_{\rm b\parallel} = 0.1,\ T_{\rm p\perp}/T_{\rm p\parallel} = 1.8,\ T_{\rm b\perp}/T_{\rm b\parallel} = 1. \tag{8}$$

This choice is comparable with the proton properties in the fast solar wind at $R_0 \sim 0.3$ AU (but no alpha particles and other minor ions are considered here for simplicity). The characteristic time is chosen to be $t_e = 10^4/\omega_{\rm cp0}$, which is about 10 times faster than in the solar wind. The system of Equation (8), is marginally stable with respect to all the relevant instabilities (see below).

3.2. Waves

The wave activity is initially on the noise level which is negligible owing to the large number of particles per cell. Consequently, the system follows the double adiabatic prediction during the first phase. Later on, the system becomes unstable and generated waves alter the double adiabatic evolution. Figure 2 displays the evolution of the wave spectra: The top panel shows the fluctuating magnetic field $\delta B^2/B_0^2$ as a function of time (solid line). The dashed line denotes the fluctuating magnetic field with oblique propagation, $|\theta_{kB}| > 30^{\rm o}$. The middle and bottom panels display gray scale plots of the fluctuating magnetic field δB as a function of time and wave vector k and as a function of time and propagation angle θ_{kB}, respectively.

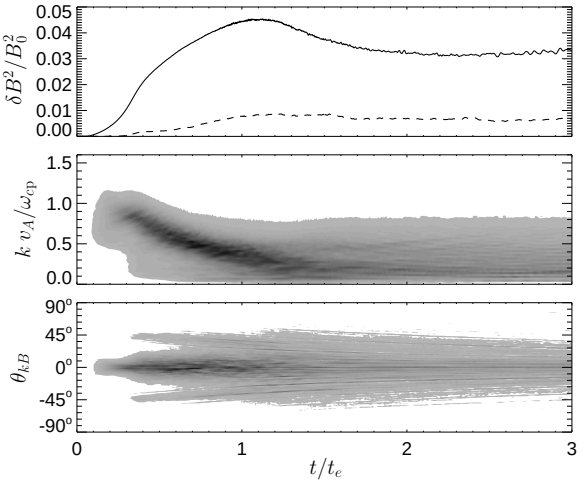

Figure 2. Evolution of the wave spectra: (top) Fluctuating magnetic field $\delta B^2/B_0^2$ (solid line) as a function of time. The dashed line shows the fluctuating magnetic field at oblique propagation with $|\theta_{kB}| > 30^{\rm o}$. Gray scale plots of the fluctuating magnetic field δB as a function of time and wave vector k (middle panel) and as a function of time and propagation angle θ_{kB} (bottom panel).

Figure 2 clearly demonstrates that soon after the beginning of the simulation electromagnetic waves are generated, first at a quasi-parallel propagation with wave vectors about 0.5–$1.1v_A/\omega_{\rm cp}$, presumably due to the parallel magnetosonic instability, and, later, oblique waves appear with lower amplitudes and with wave vectors about 0.1–$0.5v_A/\omega_{\rm cp}$, probably due to the oblique Alfvén instability. To understand better properties of the generated waves let us look at the density fluctuations. Figure 3 display the evolution of the density fluctuations in a format similar to Figure 2. The top panel of Figure 3 shows the fluctuating total proton density $\delta n^2/n_0^2$ as a function of time, whereas, the middle and bottom panels display a gray scale plot of the fluctuating total proton density δn as a function of time and wave vector k and as a function of time and propagation angle θ_{kB}, respectively.

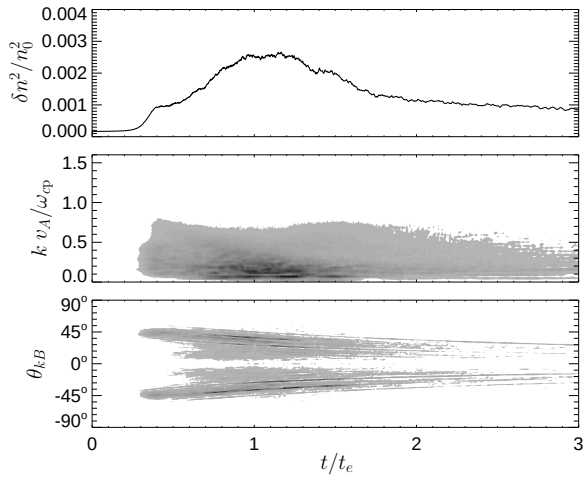

Figure 3. Evolution of the density fluctuations: (top) Fluctuating proton density $\delta n^2/n_0^2$ as a function of time. Gray scale plots of the fluctuating density δn as a function of time and wave vector k (middle panel) and as a function of time and propagation angle θ_{kB} (bottom panel).

Figure 3 shows that the quasi-parallel waves are essentially incompressible in agreement with the linear expectations whereas the oblique waves are weakly compressible. Further analysis indicates that the oblique waves have comparable transverse magnetic components $\delta B_y \sim \delta B_z \sim \delta B_x$ and that the parallel component δB_x evolves similarly to δn (see Figure 3) and has similar amplitudes $\delta B_x^2/B_0^2 \simeq \delta n^2/n_0^2$.

The top panels of Figures 2 and 3 also indicate that the oblique waves grow in two stages with a first saturation around $t \sim 0.4t_e$ and a second saturation around $t \sim t_e$. When speaking about saturation, it is important to note that both the background and the fluctuating magnetic fields decrease with time with generally different rates. The background magnetic field decreases following Equation (5) and the rate for the fluctuating magnetic fields depends on the wave properties [e.g., for low-frequency Alfvén waves one expects WKB evolution, cf., *Liewer et al.*, 2001; *Hellinger et al.*, 2005]. Furthermore, the wave modes which have been generated may (and likely will eventually) become damped/stabilized [*Matteini et al.*, 2006; *Rosin et al.*, 2011].

3.3. Velocity distribution functions

Further investigation of instabilities (or other processes) which are responsible for the observed waves it is necessary to investigate the evolution of the proton velocity distribution function. Figure 4 displays the proton distribution function at three times: (top panels) $t = 0.2t_e$, (middle panels) $t = t_e$, and (bottom panels) at $t = 3t_e$. The left panels show the total proton distribution function, the middle panels shows the distribution function of protons which initially formed the core while the right panels shows the distribution function of protons which initially formed the bean population. Figure 4 shows that the proton velocity distribution function is strongly modified owing to the interaction between protons and the generated waves. The beam particles are clearly slowed down. The perpendicular cooling expected from the double adiabatic prediction concerns only a portion of the proton distribution with roughly $|v_\parallel| \lesssim v_A$. The superalfvénic protons are heated in the perpendicular direction for both the beam and core populations. This is consistent with the quasi-linear predictions for the parallel magnetosonic and oblique Alfvén instabilities for the standard and anomalous cyclotron resonances. Furthermore, there are indications of a formation of a quasi-linear plateau due to the Landau resonance.

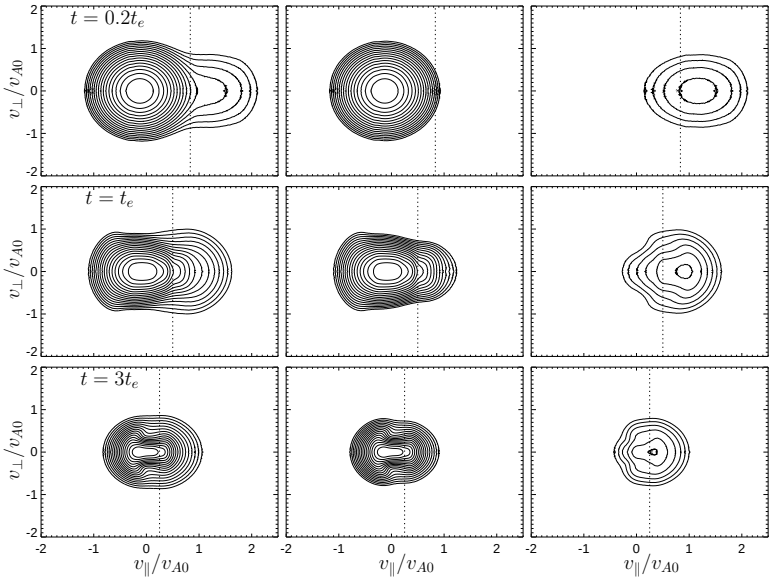

Figure 4. Proton velocity distribution functions as functions of $v_\parallel$ and $v_\perp$ (normalized to the initial Alfvén velocity v_{A0}) at (top panels) $t = 0.2t_e$, (middle panels) $t = t_e$, and (bottom panels) at $t = 3t_e$. Left panels show the total distribution function, the middle panels shows the distribution function of particles which initially formed the core while right panels shows the distribution function of particles which initially formed the bean population. Dashed lines displays the local Alfvén velocity v_A.

The complex proton velocity distribution function presents a problem when we attempt to separate the core and beam particles. In the code the core and beam populations are treated as separated species and we can determine their mean velocities and temperatures. In reality, however, it is impossible to determine the origin of a given proton. One possibility how to characterize the proton velocity distribution function is to fit it by a given analytical form. Here we fit the proton velocity distribution function as a superposition of two bi-Maxwellian distribution drifting with respect to each other along the ambient magnetic field [cf., *Goldstein et al.*, 2000]. We expect that such a fit would work at least at the beginning of the simulation as the initial velocity distribution function has this form.

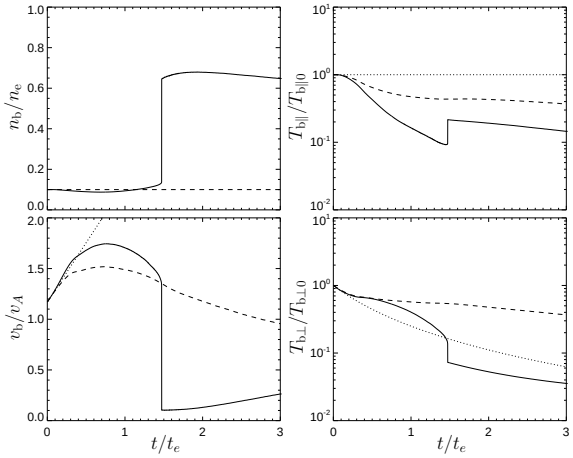

Figure 5. Evolution of the beam properties: (top left) number density, n_b, (bottom left) mean velocity, v_b, (top right) parallel, and (bottom right) perpendicular temperatures, $T_{\mathrm{b}\parallel}$ and $T_{\mathrm{b}\perp}$, as functions of time. Solid lines show results of a fit of the total proton distribution function as a sum of two bi-Maxwellian velocity distribution functions. Dashed lines show moments calculated from protons which initially formed the beam. Dotted lines denote the double-adiabatic prediction.

Figure 5 shows the evolution of the beam properties obtained from the fit (solid lines) compared to the moments calculated from protons which initially formed the beam (dashed lines). Figure 5 displays (top left) number density, $n_{\rm b}$, (bottom left) mean velocity, $v_{\rm b}$, (top right) parallel, and (bottom right) perpendicular temperatures, $T_{\rm b\parallel}$ and $T_{\rm b\perp}$, as functions of time. For a comparison the dotted lines denote the double-adiabatic prediction. Figure 5 shows that initially the fit and the moments give similar results following the double adiabatic prediction. As the important wave activity develops the double adiabatic prediction is broken, beam protons slow down and are heated in the perpendicular direction while they cool in the parallel directions. During this time the fitted results departs considerably from the calculated moments and after $t \gtrsim 1.5t_e$ there is a jump in the fitted results which indicates that the proton velocity distribution cannot be at later times characterized as a superposition of two bi-Maxwellian distributions (see Figure 4).

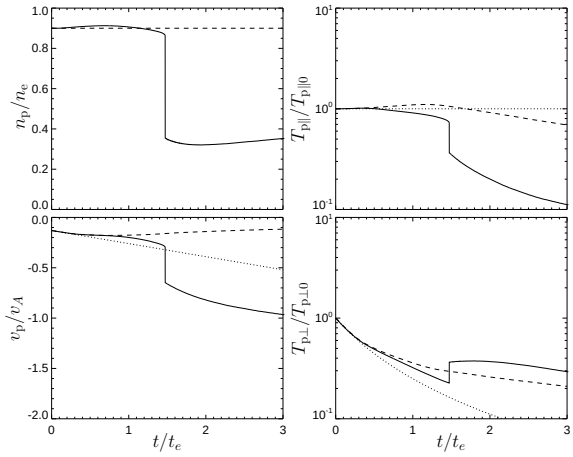

Figure 6. Evolution of the proton core properties: (top left) number density, $n_{\rm b}$, (bottom left) mean velocity, $v_{\rm p}$, (top right) parallel, and (bottom right) perpendicular temperatures, $T_{\rm p\parallel}$ and $T_{\rm p\perp}$, as functions of time. Solid lines show results of a fit of the total proton distribution function as a sum of two bi-Maxwellian velocity distribution functions. Dashed lines show moments calculated from protons which initially formed the core. Dotted lines denote the double-adiabatic prediction.

As for the core protons, Figure 6 shows the corresponding plot for the evolution of the core obtained from the fit (solid lines) compared to the moments calculated from protons which initially formed the beam (dashed lines). Figure 6 shows (top left) number density, $n_{\rm b}$, (bottom left) mean velocity, $v_{\rm p}$, (top right) parallel, and (bottom right) perpendicular temperatures, $T_{\rm p\parallel}$ and $T_{\rm p\perp}$, as functions of time in the same format as in Figure 5. For comparison the dotted lines denote the double-adiabatic prediction. Figure 6 shows that initially the fit and the moments give similar results and follow the double adiabatic prediction. As the important wave activity appears the core protons are weakly accelerated, cooled in the parallel direction and heated in the perpendicular one. The fitted results then departs considerably from the calculated moments and after $t \gtrsim 1.5t_e$, there is the jump in the fitted results.

3.4. Instabilities and nonlinear effects

The fitted results now may be used to estimate the linear stability of the proton distribution. It turns out, however, that the linear prediction based on the fitted results may strongly depart from the linear calculation based on the velocity distribution since the relevant instabilities are resonant. Figure 7 shows the linear prediction, the maximum growth rate $\gamma_{\rm max}$ as a function of time for the relevant instabilities. The top left panel shows $\gamma_{\rm max}$ the parallel magnetosonic/fire hose instability for waves propagating along the beam, $v_{\rm bp}k_\parallel\omega > 0$. The bottom left panel shows $\gamma_{\rm max}$ for the parallel fire hose instability for the propagation against the beam, $v_{\rm bp}k_\parallel\omega < 0$. The top right panel shows $\gamma_{\rm max}$ for the oblique Alfvén instability. Finally, the bottom right panel shows $\gamma_{\rm max}$ for the parallel proton cyclotron instability for the propagation along the beam. The solid lines show the results for the two bi-Maxwellian fit of the proton velocity distribution function (the results are only shown for $t \lesssim 1.5t_e$, see above for the problems with the fitting procedure) whereas the dots display the linear prediction calculated from the actual distribution function. For the parallel propagating instabilities Equation (A4) is used (with the appropriate sign) whereas for the oblique Alfvén instability the general from of the dispersion relation, Equation (A1), is used (in the infinite sum only the subset $-10 \le n \le 10$ is taken into account; for more details see Appendix A).

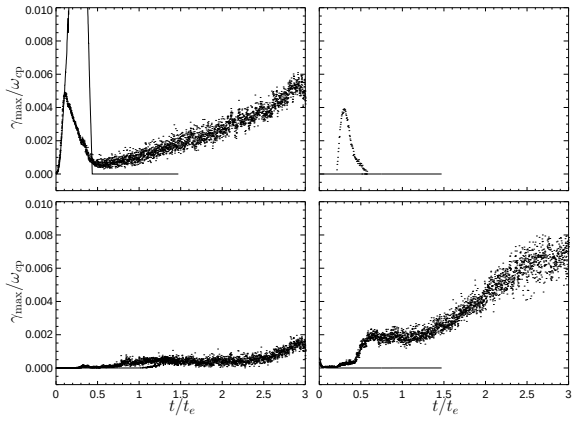

Figure 7. Maximum growth rate $\gamma_{\rm max}$ as a function of time for the relevant instabilities: (top left) the parallel magnetosonic/fire hose instability for the propagation along the beam, (bottom left) parallel fire hose instability for the propagation against the beam, (top right) oblique Alfvén instability, and (bottom right) parallel proton cyclotron instability for the propagation along the beam. The solid lines show the results for the two bi-Maxwellian fit of the proton velocity distribution function whereas the dots display the linear prediction calculated from the actual distribution function.

Figure 7 (top left panel) shows that the system is initially stable with respect to the parallel magnetosonic instability but becomes rapidly unstable. The proton velocity distribution function remains nearly bi-Maxwellian and the predic-

tion based on the bi-Maxwellian fit is close to that based on the full velocity distribution function. The two predictions soon substantially differ starting at $t \simeq 0.1t_e$ where the maximum growth rate based on the velocity distribution function starts to decrease whereas the prediction based on the fit continues to increase (it reaches the maximum $\gamma \simeq 0.02\omega_{\rm cp}$ at $t \simeq 0.3t_e$). This discrepancy is likely owing to the resonant wave-particle interaction (see Figure 4, top panels). The system seems to become nearly stabilized at $t \simeq 0.5t_e$; later on the maximum growth rate increases again. In this case it is rather the parallel fire hose instability as the proton velocity distribution function exhibit rather a temperature anisotropy than a drifting beam population (see Figure 4) although the distinction between the two instabilities is not clear.

Figure 7 (top right panel) shows that the system is also initially stable with respect to the oblique Alfvén instability. This instability appears later than the parallel magnetosonic one ($t \simeq 0.2t_e$) when the proton velocity distribution function is importantly affected by the wave-particle interactions (see Figure 4, top panels). In this case the linear prediction based on the fit does not exhibit an unstable solution contrary to the prediction based on the velocity distribution function which gives the maximum growth rate for the oblique Alfvén instability with magnitudes similar to those of the parallel magnetosonic instability. The linear prediction based on the velocity distribution function gives the maximum growth rate for a mode with a wave vector and an angle compatible with the properties of the oblique wave activity observed in the simulations at the same time (see Figures 2 and 3). The appearance of the oblique waves likely contributes to the stabilization of the magnetosonic instability. After the stabilization of the oblique Alfvén instability at $t \simeq 0.5t_e$ the maximum growth rate of the parallel magnetosonic/fire hose instability starts to increase.

The oblique Alfvén instability may explain the first growth of the oblique waves which saturates at $t \simeq 0.4t_e$ but cannot explain the second growth and saturation at $t \simeq t_e$ (see Figure 3). It is possible that some other oblique instability [cf., *Daughton and Gary*, 1998] appears then but we have not been able to find it. This does not exclude a possibility of another instability since the parameter space is very large but it may indicate that these oblique waves grow due to nonlinear effects, for example a wave-wave interaction. To test if there exists a three-wave interaction, we have calculated the bicoherence $b(\boldsymbol{k}_1, \boldsymbol{k}_2)$ [*Kim and Powers*, 1979] of the discrete-Fourier-transformed B_z component of the magnetic field as

$$b(\boldsymbol{k}_1, \boldsymbol{k}_1) = \frac{\left|\left\langle B_z(\boldsymbol{k}_1) B_z(\boldsymbol{k}_2) \overline{B_z(\boldsymbol{k}_1 + \boldsymbol{k}_2)} \right\rangle\right|}{\left\langle \left| B_z(\boldsymbol{k}_1) B_z(\boldsymbol{k}_2) \overline{B_z(\boldsymbol{k}_1 + \boldsymbol{k}_2)} \right| \right\rangle} \quad (9)$$

where $\langle\rangle$ denotes time averaging. This bicoherence b is a four-dimensional array which is difficult to analyze; taking different two-dimensional cuts of the four-dimensional space $(\boldsymbol{k}_1, \boldsymbol{k}_2)$ we have found important phase coherences indicating a three-wave interactions between one oblique mode and two quasi-parallel modes. The bicoherence is important for $t \gtrsim 0.4t_e$ which suggests that secondary growth of the oblique waves is mainly driven by the wave-wave interaction. The initial growth of oblique waves seems to be rather related to the oblique Alfvén instability with a possible contribution of the three-wave interaction.

Figure 7 (bottom right panel) shows an interesting phenomenon. The proton cyclotron instability (for the propagation along the beam) is initially weakly unstable ($\gamma_{max} \simeq 3 \cdot 10^{-4}\omega_{\rm cp}$) owing to the core temperature anisotropy. Because of the perpendicular cooling this instability is rapidly stabilized before it can drive an important wave activity. This instability, however, appears later on, during the stabilization of the oblique Alfvén instability. The destabilization of the proton cyclotron instability is therefore likely caused by the resonant heating of the core protons by the Alfvén waves driven by the oblique Alfvén instability in agreement with quasi-linear predictions (see Figure 1 and the corresponding text). The proton cyclotron instability remains unstable long after the oblique instability becomes stabilized. This is possibly because the oblique waves are present in the simulation long after the saturation. Moreover, the proton velocity distribution is further influenced by the parallel magnetosonic/fire hose instability and the nonlinear wave-wave interactions at later times which may further influence the linear stability of the system.

Figure 7 (bottom left panel) shows that the anti-parallel fire hose instability is essentially stable during most of the simulation. This instability seems to appear with small growth rates near the end of the simulation, possibly as a result of the expansion and the parallel proton heating due to the proton cyclotron waves and/or due to nonlinear wave-wave interactions. Finally, we note a relatively large scatter of the calculated maximum growth rates based on the velocity distribution function (Figure 7, points) which indicates that the precision of the calculation of the order of $10^{-4}\omega_{\rm cp}$.

3.5. Macroscopic view

The bean-core separation of the proton velocity distribution function is almost impossible during the later stages of the simulation. For a comparison of the simulation results with observations it is therefore interesting to look at the moments of the total proton velocity distribution function. Figure 8 (top panels) shows the evolution of the total/effective (left) parallel and (right) perpendicular temperatures, $T_\parallel$ and $T_\perp$, respectively, as functions of time. For comparison the dotted lines denote the double-adiabatic prediction. The combined actions of the parallel cooling of both the populations and of the beam deceleration with respect to the core leads to an important decrease of the total parallel temperature. The perpendicular heating of the two populations contributes to a decrease of the total perpendicular temperature slower than what is expected from the double adiabatic prediction.

To characterize the skewness of the proton velocity distribution function owing to presence of the beam population let us look at the proton heat flux. Figure 8 (bottom panels) shows the evolution of the (left) parallel and (right) per-

pendicular components of the proton heat flux, $q_\parallel$ and $q_\perp$, respectively. The two heat fluxes are normalized to the corresponding parallel and perpendicular saturation heat fluxes

$$q_{\mathrm{sat}\parallel} = \frac{n(k_B T_\parallel)^{3/2}}{m^{1/2}} \text{ and } q_{\mathrm{sat}\perp} = \frac{n k_B^{3/2} T_\parallel^{1/2} T_\perp}{m^{1/2}}, \quad (10)$$

respectively. Initially, the system follows the double-adiabatic predictions and the ratio between the heat fluxes and the corresponding saturation values remain constant. The deceleration of the beam with respect to the core (and the parallel cooling) leads to a decrease of the parallel heat flux component with respect to the saturation value but they have values of the same order all the time. The perpendicular heat flux component increases with respect to the saturation value owing to the perpendicular heating but later on it decreases as the deceleration becomes the dominant effect.

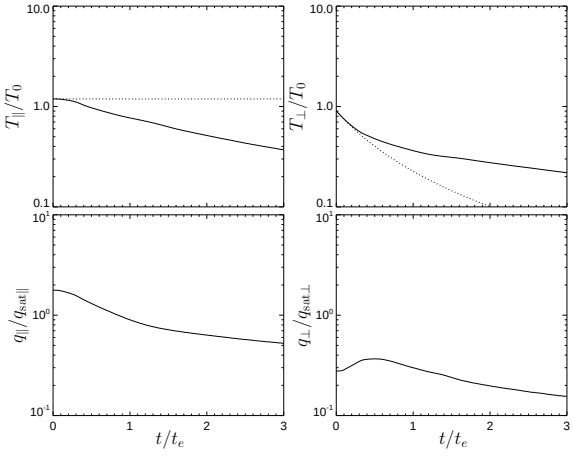

Figure 8. Top panels: Total (left) parallel, and (right) perpendicular temperatures, $T_\parallel$ and $T_\perp$ (normalized to the initial mean total temperature $T_0 = (T_{\parallel 0} + 2T_{\perp 0})/3$), as functions of time. Bottom panels: (left) parallel and (right) perpendicular components of the proton heat flux, $q_\parallel$ and $q_\perp$ (normalized to the corresponding saturation heat flux, $q_{\mathrm{sat}\parallel}$ and $q_{\mathrm{sat}\perp}$, respectively), as functions of time. Dotted lines denote the corresponding double-adiabatic predictions.

4. Discussion

In this paper we have presented results of a 2-D hybrid expanding box simulation for the proton beam-core system in the fast solar wind with initial proton parameters comparable with the Helios observations at 0.3 AU. The HEB simulation exhibits a complicated evolution. The system is most of the time marginally unstable with respect to (at least) four different instabilities which determine the system evolution counteracting some effects of the expansion and competing with or driving each other. The expansion with the strictly radial magnetic field leads to a decrease of the ratio between the perpendicular and parallel proton temperatures as well as to an increase of the ratio between the beam-core differential velocity and the local Alfvén velocity. In this way the expansion creates a free energy for many different instabilities. For the chosen initial condition the expanding system becomes rapidly unstable with respect to the parallel magnetosonic instability. This instability saturates rapidly in a quasi-linear manner by scattering/heating in the perpendicular direction the resonant particles through the anomalous cyclotron resonance while only weakly decelerating these particles with respect to the core in agreement with previous standard simulation results [*Daughton et al.*, 1999]. This evolution leads to destabilization of the competing oblique Alfvén instability which is more efficient in reducing the drift velocity because the generated waves interact with protons through all the three resonances. The oblique Alfvén instability saturates and becomes stabilized while the parallel magnetosonic instability or rather the parallel fire hose instability becomes unstable. At the same time the perpendicular (resonant) scattering/heating of the core protons leads to destabilization of the parallel proton cyclotron instability. Such a simple quasi-linear picture is however modified by nonlinear (wave-wave) interactions which appear around the first saturation of the oblique Alfvén instability. The relevance of the quasi-linear approximation becomes then questionable; this is a general problem of the weak turbulence in the magnetized collisionless plasmas [cf., *Aamodt and Drummond*, 1964; *Sugaya*, 1991] which needs further theoretical and modeling work. The chain of the different resonant instabilities and nonlinear effects leads to large modifications of the proton velocity distribution function so that except a short initial period the distribution function cannot be simply described as a superposition of two bi-Maxwellian distribution functions and the linear analysis must be performed using the local velocity distribution function (but again the relevance of the linear prediction at the nonlinear stage is questionable).

On the macroscopic level the instabilities lead to large departures from the double adiabatic predictions, the wave-particle interactions cause an efficient isotropization of effective temperatures. The wave-particle interactions also reduce the proton heat flux. The present simulation started with the parallel heat flux comparable to the saturation one and these two heat fluxes remained comparable during whole the simulation.

The simulation model used in this paper does not fully describe the complex properties of the solar wind. We assumed the strictly radial magnetic field for simplicity; this nominally represents the polar regions but is also compatible with the inner heliosphere below 1 AU where the magnetic field is predominantly radial. The chosen characteristic expansion time is about ten times faster than in the solar wind, the model does not include the turbulence/wave activity present in the solar wind and minor ions as alpha particles are not considered. The model, however, self-consistently resolves the competition between the expansion and kinetic instabilities. The presented simulation results suggest that the kinetic instabilities are partly responsible for the proton perpendicular heating and parallel cooling in the fast solar wind as observed by Helios [*Marsch and Richter*, 1987; *Hellinger et al.*, 2011]. This paper also confirms that the linear prediction for resonant instabilities generally needs to be calculated from the full distribution function [cf., *Dum*

et al., 1980]; this property may explain observations where instability analyses based on simplified models of the proton velocity distribution function indicate strong linear growth rates [*Marsch and Livi*, 1987; *Hellinger et al.*, 2006] (to say nothing about nonlinear effects).

Appendix A: Linear theory

The linear dispersion relation $\omega = \omega(\boldsymbol{k})$ in the magnetized collisionless (non relativistic) plasma is given by

$$\det\mathbf{D}(\boldsymbol{k},\omega) = 0 \tag{A1}$$

where the dispersion matrix $\mathbf{D}$ is given by

$$\begin{aligned}\mathbf{D} &= \left(\frac{k^2c^2+\omega_p^2}{\omega^2} - 1\right)\mathbf{1} - \boldsymbol{k}\boldsymbol{k}\frac{c^2}{\omega^2} \\ &- \sum_{\mathrm{s}}\frac{\omega_{ps}^2}{\omega^2 n_{\mathrm{s}}}\sum_{n=-\infty}^{\infty}\int\frac{k_\parallel\frac{\partial f_{\mathrm{s}}}{\partial v_\parallel} + n\frac{\omega_{cs}}{v_\perp}\frac{\partial f_{\mathrm{s}}}{\partial v_\perp}}{\omega - k_\parallel v_\parallel - n\omega_{cs}}\mathbf{T}_{ns}\,\mathrm{d}^3v\end{aligned} \tag{A2}$$

Where $\mathbf{T}_{ns}$ are Hermitian matrices

$$\mathbf{T}_{ns} = \begin{pmatrix} \frac{n^2\omega_{cs}^2}{k_\perp^2}J_n^2 & -\frac{in\omega_{cs}}{k_\perp}v_\perp J_n J_n' & \frac{n\omega_{cs}}{k_\perp}v_\parallel J_n^2 \\ \frac{in\omega_{cs}}{k_\perp}v_\perp J_n J_n' & v_\perp^2 J_n'^2 & iv_\parallel v_\perp J_n J_n' \\ \frac{n\omega_{cs}}{k_\perp}v_\parallel J_n^2 & -iv_\parallel v_\perp J_n J_n' & v_\parallel^2 J_n^2 \end{pmatrix} \tag{A3}$$

J_n and J_n' being the Bessel functions of the fist kind and their derivatives, respectively, of the integer order n with the argument $k_\perp v_\perp/\omega_{cs}$ (for the definitions of all symbol used here see Appendix C).

At the parallel propagation the dispersion relation splits to an electrostatic branch and two electromagnetic branches with left- and right-handed circular polarization:

$$\frac{k_\parallel^2c^2+\omega_p^2}{\omega^2} - \sum_{\mathrm{s}}\frac{\omega_{ps}^2}{\omega^2 n_{\mathrm{s}}}\int\frac{v_\perp^2}{2}\frac{k_\parallel\frac{\partial f_{\mathrm{s}}}{\partial v_\parallel} \mp \frac{\omega_{cs}}{v_\perp}\frac{\partial f_{\mathrm{s}}}{\partial v_\perp}}{\omega - k_\parallel v_\parallel \pm \omega_{cs}}\,\mathrm{d}^3v = 1 \tag{A4}$$

The above expressions, Eqs. (A1,A4) are valid only for $\gamma = \Im\omega > 0$ and for $\gamma \le 0$ must be analytically continued.

The linear dispersion relation must be generally solved numerically. In the case when particle velocity distribution functions may be considered as bi-Maxwellian distributions drifting along the ambient magnetic field the integration over velocities in the dispersion relations may be performed analytically which leads to expressions involving the plasma dispersion function [*Fried and Conte*, 1961] and (at oblique propagation) modified Bessel functions [cf., *Stix*, 1992].

For a general distribution function the integration must be performed numerically even in the case of analytical form [cf., *Wong et al.*, 1991]. In the case of a velocity distribution function obtained on a grid from numerical simulation (using the particle-in-cell scheme) or a discrete velocity distribution function observed in situ [*Dum et al.*, 1980] the solving the dispersion relation is more complicated. In this case it is better to remove the derivatives of the distribution function via the integration *per partes*. For instance, in the case of the parallel propagation, the relation, Equation (A4) reads

$$\begin{aligned}&\frac{k_\parallel^2c^2+\omega_p^2}{\omega^2} + \sum_{\mathrm{s}}\frac{\omega_{ps}^2}{\omega^2 n_{\mathrm{s}}}\int\frac{v_\perp^2}{2}\frac{k_\parallel^2 f_{\mathrm{s}}}{(\omega - k_\parallel v_\parallel \pm \omega_{cs})^2}\,\mathrm{d}^3v \\ &\pm \sum_{\mathrm{s}}\frac{\omega_{ps}^2}{\omega^2 n_{\mathrm{s}}}\int\frac{\omega_{cs}f_{\mathrm{s}}}{\omega - k_\parallel v_\parallel \pm \omega_{cs}}\,\mathrm{d}^3v = 1.\end{aligned} \tag{A5}$$

Similar but more complicated expressions one obtains in the general case, Equation (A2). For the velocity distribution function obtained on a fine grid, one can approximate the integral by a simple summation over the grid; this is the method used in this paper. We have, however, encountered numerical problems for very weak growth rates. After the integration/summation over $v_\perp$ one gets to evaluate this type of integral:

$$\int_{-\infty}^{\infty}\frac{\tilde f(v_\parallel)}{\omega - k_\parallel v_\parallel - n\omega_{cs}}\mathrm{d}v_\parallel. \tag{A6}$$

Close to $\gamma = \Im\omega = 0$ the resonances pose numerical problems. One possibility to remedy this problem is to move the integration contour below the real line to

$$\int_{-\infty-i\epsilon}^{\infty-i\epsilon}\frac{\tilde f(v_\parallel)}{\omega - k_\parallel v_\parallel - n\omega_{cs}}\mathrm{d}v_\parallel \tag{A7}$$

for a small $\epsilon > 0$. This procedure requires an analytical continuation of $\tilde f(v_\parallel)$ which may be approximated using the real derivative $\tilde f(v_\parallel - i\epsilon) = \tilde f(v_\parallel) - i\epsilon\partial\tilde f/\partial v_\parallel$.

Appendix B: Quasilinear theory

Assuming the quasi-linear approximation, a superposition of linear waves [*Kennel and Engelmann*, 1966]

$$\boldsymbol{E}^{(1)} = \sum_{\boldsymbol{k}}\delta\boldsymbol{E}(\boldsymbol{k},\omega)\,\mathrm{e}^{i\boldsymbol{k}\cdot\boldsymbol{x}-i\omega t} \tag{B1}$$

$$f_{\mathrm{s}}^{(1)} = \sum_{\boldsymbol{k}}\delta f_{\mathrm{s}}(\boldsymbol{v},\boldsymbol{k},\omega)\,\mathrm{e}^{i\boldsymbol{k}\cdot\boldsymbol{x}-i\omega t} \tag{B2}$$

$$\dots$$

which are solutions of the linear dispersion

$$\mathbf{D}(\boldsymbol{k},\omega)\cdot\delta\boldsymbol{E}(\boldsymbol{k},\omega) = 0 \tag{B3}$$

based on the instantaneous velocity distribution functions f_{s} which in turn is assumed to vary owing to the second order effects averaged over the space, phase and (fast) time,

$$\frac{\partial f_{\mathrm{s}}}{\partial t} = -\frac{q_{\mathrm{s}}}{m_{\mathrm{s}}}\left\langle\left(\boldsymbol{E}^{(1)} + \boldsymbol{v}\times\boldsymbol{B}^{(1)}\right)\cdot\frac{\partial f_{\mathrm{s}}^{(1)}}{\partial\boldsymbol{v}}\right\rangle. \tag{B4}$$

The second order effects lead to the diffusion equation

$$\begin{aligned}\frac{\partial f_{\mathrm{s}}}{\partial t} &= \frac{\partial}{\partial v_\parallel}\left(D_{\parallel\parallel\mathrm{s}}\frac{\partial f_{\mathrm{s}}}{\partial v_\parallel} + D_{\parallel\perp\mathrm{s}}\frac{\partial f_{\mathrm{s}}}{\partial v_\perp}\right) \\ &+ \frac{1}{v_\perp}\frac{\partial}{\partial v_\perp}v_\perp\left(D_{\perp\parallel\mathrm{s}}\frac{\partial f_{\mathrm{s}}}{\partial v_\parallel} + D_{\perp\perp\mathrm{s}}\frac{\partial f_{\mathrm{s}}}{\partial v_\perp}\right).\end{aligned} \tag{B5}$$

where the diffusion coefficient can be given the following explicit form

$$D_{\parallel\parallel\mathrm{s}} = \sum_{\boldsymbol{k}}\sum_{n=-\infty}^{\infty} \frac{q_\mathrm{s}^2}{m_\mathrm{s}^2}\frac{1}{k_\perp^2|\omega|^2}\frac{\gamma}{|\omega - k_\parallel v_\parallel - n\omega_{\mathrm{cs}}|^2}\times$$
$$\Re\Big[|\delta E_x|^2 n^2 J_n^2 k_\parallel^2 \omega_{\mathrm{cs}}^2 + |\delta E_y|^2 (J_n')^2 k_\parallel^2 k_\perp^2 v_\perp^2 + |\delta E_z|^2 J_n^2 k_\perp^2 |\omega - n\omega_{\mathrm{cs}}|^2 + 2i\delta E_x \overline{\delta E}_y n J_n J_n' k_\parallel^2 k_\perp \omega_{\mathrm{cs}} v_\perp - 2i(\overline{\omega} - n\omega_{\mathrm{cs}})\delta E_y \overline{\delta E}_z J_n J_n' k_\parallel k_\perp^2 v_\perp + 2(\overline{\omega} - n\omega_{\mathrm{cs}})\delta E_x \overline{\delta E}_z n J_n^2 k_\parallel k_\perp \omega_{\mathrm{cs}}\Big] \quad \text{(B6)}$$

$$D_{\parallel\perp\mathrm{s}} = \sum_{\boldsymbol{k}}\sum_{n=-\infty}^{\infty} \frac{q_\mathrm{s}^2}{m_\mathrm{s}^2}\frac{n\omega_{\mathrm{cs}}}{k_\perp^2 v_\perp|\omega|^2}\frac{\gamma}{|\omega - k_\parallel v_\parallel - n\omega_{\mathrm{cs}}|^2}\times$$
$$\Re\Big[|\delta E_x|^2 n^2 J_n^2 k_\parallel \omega_{\mathrm{cs}}^2 + |\delta E_y|^2 (J_n')^2 k_\parallel k_\perp^2 v_\perp^2 + |\delta E_z|^2 J_n^2 k_\perp^2 v_\parallel \left(2\omega_r - k_\parallel v_\parallel - 2n\omega_{\mathrm{cs}}\right) + 2i\delta E_x \overline{\delta E}_y n J_n J_n' k_\parallel k_\perp v_\perp \omega_{\mathrm{cs}} - 2i(\overline{\omega} - n\omega_{\mathrm{cs}})\delta E_y \overline{\delta E}_z J_n J_n' k_\perp^2 v_\perp + 2(\overline{\omega} - n\omega_{\mathrm{cs}})\delta E_x \overline{\delta E}_z n J_n^2 k_\perp \omega_{\mathrm{cs}}\Big] \quad \text{(B7)}$$

$$D_{\perp\parallel\mathrm{s}} = \sum_{\boldsymbol{k}}\sum_{n=-\infty}^{\infty} \frac{q_\mathrm{s}^2}{m_\mathrm{s}^2}\frac{k_\parallel}{k_\perp^2 v_\perp|\omega|^2}\frac{\gamma}{|\omega - k_\parallel v_\parallel - n\omega_{\mathrm{cs}}|^2}\times$$
$$\Re\Big[|\delta E_x|^2 n^2 J_n^2 \omega_{\mathrm{cs}}^2 \left(2\omega_r - 2k_\parallel v_\parallel - n\omega_{\mathrm{cs}}\right) + |\delta E_y|^2 (J_n')^2 k_\perp^2 v_\perp^2 \left(2\omega_r - 2k_\parallel v_\parallel - n\omega_{\mathrm{cs}}\right) - |\delta E_z|^2 n J_n^2 k_\perp^2 v_\parallel^2 \omega_{\mathrm{cs}} + 2i\delta E_x \overline{\delta E}_y n J_n J_n' k_\perp v_\perp \omega_{\mathrm{cs}} \left(2\omega_r - 2k_\parallel v_\parallel - n\omega_{\mathrm{cs}}\right) - 2i(\omega - k_\parallel v_\parallel)\delta E_y \overline{\delta E}_z J_n J_n' k_\perp^2 v_\parallel v_\perp + 2(\omega - k_\parallel v_\parallel)\delta E_x \overline{\delta E}_z n J_n^2 k_\perp v_\parallel \omega_{\mathrm{cs}}\Big] \quad \text{(B8)}$$

$$D_{\perp\perp\mathrm{s}} = \sum_{\boldsymbol{k}}\sum_{n=-\infty}^{\infty} \frac{q_\mathrm{s}^2}{m_\mathrm{s}^2}\frac{1}{k_\perp^2 v_\perp^2|\omega|^2}\frac{\gamma}{|\omega - k_\parallel v_\parallel - n\omega_{\mathrm{cs}}|^2}\times$$
$$\Re\Big[|\delta E_x|^2 n^2 J_n^2 \omega_{\mathrm{cs}}^2 |\omega - k_\parallel v_\parallel|^2 + |\delta E_y|^2 (J_n')^2 k_\perp^2 v_\perp^2 |\omega - k_\parallel v_\parallel|^2 + |\delta E_z|^2 n^2 J_n^2 k_\perp^2 v_\parallel^2 \omega_{\mathrm{cs}}^2 + 2i\delta E_x \overline{\delta E}_y n J_n J_n' k_\perp v_\perp \omega_{\mathrm{cs}} |\omega - k_\parallel v_\parallel|^2 - 2i(\omega - k_\parallel v_\parallel)\delta E_y \overline{\delta E}_z n J_n J_n' k_\perp^2 v_\parallel v_\perp \omega_{\mathrm{cs}} + 2(\omega - k_\parallel v_\parallel)\delta E_x \overline{\delta E}_z n^2 J_n^2 k_\perp v_\parallel \omega_{\mathrm{cs}}^2\Big], \quad \text{(B9)}$$

J_n and J_n' being the Bessel functions of the fist kind and their derivatives, respectively, of the integer order n with the argument $k_\perp v_\perp/\omega_{\mathrm{cs}}$ as in the linear case. The explicit expression for the diffusion tensor are again only valid for unstable waves ($\gamma > 0$).

Appendix C: Glossary

Here subscripts $\perp$ and $\parallel$ denote the perpendicular and parallel directions with respect to the ambient magnetic field $\boldsymbol{B}_0$, $B_0 = |\boldsymbol{B}_0|$ denotes its the magnitude; $\boldsymbol{v}$ denotes a velocity, $v = |\boldsymbol{v}|$ being its magnitude, and $v_\parallel$ and $v_\perp$ denote magnitude of the velocity components parallel and perpendicular to $\boldsymbol{B}_0$, respectively; t denotes the time. Here subscript s denotes different species (e: electrons, p: core protons, and b: beam protons); subscript 0 denotes initial values. Here f_s denotes the velocity distribution function, n_s denotes the number density $n_\mathrm{s} = \int f\,\mathrm{d}^3v$ and mean parallel velocities v_s are given as $v_\mathrm{s} = \int v_\parallel f_\mathrm{s}\,\mathrm{d}^3v/n_\mathrm{s}$. The field-aligned differential velocity between the beam and core is denoted as $v_{\mathrm{bp}} = v_\mathrm{b} - v_\mathrm{p}$. The parallel and perpendicular temperatures are given as $T_{\mathrm{s}\parallel} = (m_\mathrm{s}/k_\mathrm{B}n_\mathrm{s})\int(v_\parallel - v_\mathrm{s})^2 f_\mathrm{s}\,\mathrm{d}^3v$ and $T_{\mathrm{s}\perp} = (m_\mathrm{s}/2k_\mathrm{B}n)\int v_\perp^2 f\,\mathrm{d}^3v$, respectively. Here m_s denotes the mass, k_B is the Boltzmann constant; $T_\mathrm{s} = (2T_{\mathrm{s}\perp} + T_{\mathrm{s}\parallel})/3$ is the total proton temperature. For the total proton distribution function $f = f_\mathrm{p} + f_\mathrm{b}$ we define the effective parallel and perpendicular temperatures $T_\parallel = (m_\mathrm{p}/k_\mathrm{B}n)\int(v_\parallel - \tilde{v}_\parallel)^2 f_\mathrm{s}\,\mathrm{d}^3v$ and $T_\perp = (m_\mathrm{p}/2k_\mathrm{B}n)\int v_\perp^2 f\,\mathrm{d}^3v$, respectively, where n is the total proton number density $n = n_\mathrm{p} + n_\mathrm{b}$ and $\tilde{v}_\parallel$ is the mean proton velocity, $\tilde{v}_\parallel = \int v_\parallel f\,\mathrm{d}^3v/n$. The two nonzero components of the heat flux tensor for the gyrotropic total proton distribution function f are given as $q_\parallel = m_\mathrm{p}\int(v_\parallel - \tilde{v}_\parallel)^3 f\,\mathrm{d}^3v$ and $q_\perp = (m_\mathrm{p}/2)\int(v_\parallel - \tilde{v}_\parallel)v_\perp^2 f\,\mathrm{d}^3v$. Here $\beta_{\mathrm{s}\parallel} = 2\mu_0 n_\mathrm{s} k_B T_{\mathrm{s}\parallel}/B_0^2$ is the parallel beta, $\omega_{\mathrm{cs}} = q_\mathrm{s}B_0/m_\mathrm{s}$ and $\omega_{ps} = (n_\mathrm{s}q_\mathrm{s}^2/m_\mathrm{s}\epsilon_0)^{1/2}$ denote the cyclotron and plasma frequencies, respectively, $\omega_p = \sum_\mathrm{s}\omega_{ps}$ is the total plasma frequency. In these expressions q_s denotes the charge, ϵ_0 and μ_0 denote the vacuum electric permittivity and magnetic permeability, respectively. Here v_A denotes the Alfvén velocity $v_A = B_0/(\mu_0 m_\mathrm{p} n)^{1/2}$ and c denotes the speed of light. Here, $\boldsymbol{k}$ denotes the wave vector, k its magnitude, $k_\parallel$ and $k_\perp$ its parallel and perpendicular components, respectively; i denotes the imaginary unit, ω denotes the complex frequency, $\omega_r = \Re\omega$, $\gamma = \Im\omega$ where $\Re$ and $\Im$ denote the real and imaginary part, respectively, and the overline denotes the complex conjugate, $\overline{a + ib} = a - ib$. Here R_0 denotes the initial radial distance and $t_e = R_0/v_{sw}$ is the characteristic expansion time.

Acknowledgments. Authors acknowledge the Czech grants GAAV IAA300420702 and AV0Z30420517, and the PECS contract No. 98068 from the European Space Agency. The expanding box simulation has been performed on the supercomputing facility at IAP, ASCR. The research leading to these results has received funding from the European Commissions Seventh Framework Programme (FP7/20072013) under the grant agreement SWIFF (project 263340, www.swiff.eu).

References

Aamodt, R. E., and W. E. Drummond (1964), Resonant wave-wave scattering of plasma oscillations, *Phys. Fluids*, *7*, 1816–1825.

Califano, C., P. Hellinger, E. Kuznetsov, T. Passot, P.-L. Sulem, and P. M. Trávníček (2008), Nonlinear mirror mode dynamics: Simulations and modeling, *J. Geophys. Res.*, *113*, A08219, doi:10.1029/2007JA012898.

Daughton, W., and S. P. Gary (1998), Electromagnetic proton/proton instabilities in the solar wind, *J. Geophys. Res.*, *103*, 20,613–20,620.

Daughton, W., S. P. Gary, and D. Winske (1999), Electromagnetic proton/proton instabilities in the solar wind: Simulations, *J. Geophys. Res.*, *104*, 4657–4668.

Dum, C. T., E. Marsch, and W. Pilipp (1980), Determination of wave growth from measured distribution functions and transport theory, *J. Plasma Phys.*, *23*, 91–113.

Feldman, W. C., J. R. Asbridge, S. J. Bame, and M. D. Montgomery (1973), On the origin of solar wind proton thermal anisotropy, *J. Geophys. Res.*, *78*, 6451–6468.

Fried, B. D., and S. D. Conte (1961), *The plasma dispersion function*, Academic Press, New York.

Gary, S. P. (1993), *Theory of Space Plasma Microinstabilities*, Cambridge Univ. Press, New York.

Gary, S. P., M. D. Montgomery, W. C. Feldman, and D. W. Forslund (1976), Proton temperature anisotropy instabilities in the solar wind, *J. Geophys. Res.*, *81*, 1241–1246.

Goldstein, B. E., M. Neugebauer, L. D. Zhang, and S. P. Gary (2000), Observed constraint on proton-proton relative velocities in the solar wind, *Geophys. Res. Lett.*, *27*, 53–56.

Grappin, R., M. Velli, and A. Mangeney (1993), Nonlinear-wave evolution in the expanding solar wind, *Phys. Rev. Lett.*, *70*, 2190–2193.

Hellinger, P., and P. Trávníček (2005), Magnetosheath compression: Role of characteristic compression time, alpha particle abundances and alpha/proton relative velocity, *J. Geophys. Res.*, *110*, A04210, doi: 10.1029/2004JA010687.

Hellinger, P., and P. Trávníček (2006), Parallel and oblique proton fire hose instabilities in the presence of alpha/proton drift: Hybrid simulations, *J. Geophys. Res.*, *111*, A01107, doi:10.1029/2005JA011318.

Hellinger, P., and P. Trávníček (2008), Oblique proton fire hose instability in the expanding solar wind: Hybrid simulations, *J. Geophys. Res.*, *113*, A10109, doi:10.1029/2008JA013416.

Hellinger, P., P. Trávníček, A. Mangeney, and R. Grappin (2003), Hybrid simulations of the expanding solar wind: Temperatures and drift velocities, *Geophys. Res. Lett.*, *30*, 1211, doi:10.1029/2002GL016409.

Hellinger, P., M. Velli, P. Trávníček, S. P. Gary, B. E. Goldstein, and P. C. Liewer (2005), Alfvén wave heating of heavy ions in the expanding solar wind: Hybrid simulations, *J. Geophys. Res.*, *110*, A12109, doi: 10.1029/2005JA011244.

Hellinger, P., P. Trávníček, J. C. Kasper, and A. J. Lazarus (2006), Solar wind proton temperature anisotropy: Linear theory and WIND/SWE observations, *Geophys. Res. Lett.*, *33*, L09101, doi: 10.1029/2006GL025925.

Hellinger, P., L. Matteini, Š. Štverák, P. M. Trávníček, and E. Marsch (2011), Heating and cooling of protons in the fast solar wind between 0.3 and 1 AU: Helios revisited, *J. Geophys. Res.*, *116*, A09105, doi: 10.1029/2011JA016674.

Kennel, C. F., and F. Engelmann (1966), Velocity space diffusion from weak plasma turbulence in a magnetic field, *Phys. Fluids*, *9*, 2377–2388.

Kim, Y. C., and E. J. Powers (1979), Digital bispectral analysis and its applications to nonlinear wave interactions, *IEEE Trans. Plasma Sci.*, *7*, 120–131.

Kivelson, M. G., and D. J. Southwood (1996), Mirror instability II: The mechanism of nonlinear saturation, *J. Geophys. Res.*, *101*, 17,365–17,372.

Liewer, P. C., M. Velli, and B. E. Goldstein (2001), Alfvén wave propagation and ion cyclotron interaction in the expanding solar wind: One-dimensional hybrid simulations, *J. Geophys. Res.*, *106*, 29,261–29,281.

Marsch, E., and S. Livi (1987), Observational evidence for marginal stability of solar wind ion beams, *J. Geophys. Res.*, *92*, 7263–7268.

Marsch, E., and A. K. Richter (1987), On the equation of state and collision time for a multicomponent, anisotropic solar wind, *Ann. Geophys.*, *5A*, 71–82.

Marsch, E., K. H. Muhlhauser, R. Schwenn, H. Rosenbauer, W. Pilipp, and F. M. Neubauer (1982), Solar-wind protons – three-dimensional velocity distributions and derived plasma parameters measured between 0.3 AU and 1 AU, *J. Geophys. Res.*, *87*, 52–72.

Matteini, L., S. Landi, P. Hellinger, and M. Velli (2006), Parallel proton fire hose instability in the expanding solar wind: Hybrid simulations, *J. Geophys. Res.*, *111*, A10101, doi:10.1029/2006JA011667.

Matteini, L., P. Hellinger, S. Landi, P. M. Travnicek, and M. Velli (2011), Ion kinetics in the solar wind: coupling global expansion to local microphysics, *Space Sci. Rev.*, in press, doi:10.1007/s11214-011-9774-z.

Matthews, A. (1994), Current advance method and cyclic leapfrog for 2D multispecies hybrid plasma simulations, *J. Comput. Phys.*, *112*, 102–116.

Montgomery, M. D., S. P. Gary, W. C. Feldman, and D. W. Forslund (1976), Electromagnetic instabilities driven by unequal proton beams in the solar wind, *J. Geophys. Res.*, *81*, 2743–2749.

Rosin, M. S., A. A. Schekochihin, F. Rincon, and S. C. Cowley (2011), A nonlinear theory of the parallel firehose and gyrothermal instabilities in a weakly collisional plasma, *Mon. Not. R. Astron. Soc.*, *413*, 7–38.

Schwartz, S. J., W. C. Feldman, and S. P. Gary (1981), The source of proton anisotropy in the high-speed solar wind, *J. Geophys. Res.*, *86*, 541–546.

Stix, T. H. (1992), *Waves in plasmas*, AIP, New York.

Sugaya, R. (1991), Velocity space diffusion due to resonant wave-wave scattering of electromagnetic and electrostatic waves in a homogeneous magnetized plasma, *J. Phys. Soc. Japan*, *60*, 3367–3385.

Tu, C.-Y., E. Marsch, and Z.-R. Qin (2004), Dependence of the proton beam drift velocity on the proton core plasma beta in the solar wind, *J. Geophys. Res.*, *109*, A05101, doi:10.1029/2004JA010391.

Wong, H. K., M. L. Goldstein, and C. W. Smith (1991), Ion cyclotron harmonic resonances driven by ion ring-beam distributions, *J. Geophys. Res.*, *96*, 285–288.

P. Hellinger, Astronomical Institute, AS CR, Prague 14131, Czech Republic. (petr.hellinger@ig.cas.cz)

P. M. Trávníček, Astronomical Institute, AS CR, Prague 14131, Czech Republic. (trav@ig.cas.cz)